RAMReS Sciences des Structures et de la Matière Vol. 10, No. 1 (2026) 93 - 103
http://publication.lecames.org/index.php/mat ISSN: 2630-1180

Metal-dependent modulation of ESIPT in a Furan-substituted chromone : A comparative DFT/TD-DFT study of Zn^{2+}, Ca^{2+}, and Cu^{2+} complexes

Abdallah Brahim Elhadj Ali[1,*], Yapara Kanabet[2], Foulla Dieudonné Platou[3], Pale Wang-Yang[4], Daniel Lissouck[5], Stève-Jonathan Koyambo-Konzapa[6]

[1]*Centre National de Recherche pour le Développement (CNRD), N'Djaména, Tchad*
[2]*Faculté de Sciences Exactes et Appliquées, Moundou, Université de Moundou, Tchad*
[3]*Faculté de Sciences Exactes et Appliquées, N'Djaména, Université de N'Djamena, Tchad*
[4]*Département de Mathématiques et Physiques, Université Saint Charles Lwanga de Sarh, Sarh, Tchad*
[5]*Laboratoire Optique et Applications, Centre de Physique Atomique Moléculaire et Optique Quantique, Faculté des Sciences, Université de Douala, B.P. 8580 Douala, Cameroun*
[6]*Laboratoire Matière, Énergie et Rayonnement (LAMER), Université de Bangui, Bangui, République Centrafricaine*

Received: 15 April 2026 / Received in revised form: 19 May 2026 / Accepted: 30 May 2026

***Abstract*:**

A comparative DFT/TD-DFT study at the B3LYP-D3BJ/def2-TZVP level, employing CPCM with methanol as solvent, was conducted to elucidate the electronic structure and photophysical properties of 2-(2-furyl)-3-hydroxychromone (FHC) and its deprotonated complexes with Zn^{2+}, Ca^{2+}, and Cu^{2+}. In the free ligand, the enol form is stabilized by an intramolecular O–H · · · O(furan) hydrogen bond. TD-DFT calculations predict a bright $S1$ state at 339 nm ($f = 0.801$). Geometry optimization of the $S1$ state for both enol and keto tautomers yields vertical emissions at 380.7 nm ($f = 0.831$) and 456.0 nm ($f = 0.847$), respectively, thereby supporting the ESIPT character of the free fluorophore. Bidentate coordination via the carbonyl (O21) and deprotonated hydroxyl (O22) oxygen atoms yields stable $[M(FHC\text{-}H)]^+$ complexes. Natural population analysis reveals significant metal-dependent ligand-to-metal charge transfer ($Cu^{2+} > Zn^{2+} > Ca^{2+}$), with notable spin delocalization in the Cu^{2+} complex (spin population ≈ 0.61 on Cu). TD-DFT predicts intense absorptions at 358 nm (Zn^{2+}, $f = 0.682$) and 382 nm (Ca^{2+}, $f = 0.783$), whereas the Cu^{2+} complex exhibits only very weak transitions in the near-infrared region, rendering it effectively optically silent in the UV-visible range. In all complexes, metal coordination induces deprotonation and eliminates the intramolecular hydrogen bond, thereby structurally suppressing the ESIPT pathway. These computational results suggest distinct metal-dependent photophysical responses that may be exploited for the development of ESIPT-based fluorescent probes, although experimental validation is required.

Keywords **:** ESIPT ; DFT/TD-DFT ; Chromone ; Metal complexes ; Charge transfer ; Fluorescent probes.

* Corresponding author:
Email address: *abdallahbrahim88@gmail.com (E.A.A. Brahim)*
https://doi.org/10.70974/mat10126093

1. Introduction

Excited-state intramolecular proton transfer (ESIPT) is a fundamental photochemical process that confers organic fluorophores with distinctive properties, including large Stokes shifts, dual emission, and high sensitivity to the local environment [1,2]. These features make ESIPT-based molecules particularly attractive for the development of fluorescent probes in biological chemistry, materials science, and analyte detection [3,4].

Among ESIPT systems, 3-hydroxychromone (3HC) derivatives are notable for their exceptional spectral sensitivity to changes in polarity, hydration, or binding partners [5]. The compound 2-(2-furyl)-3-hydroxychromone (FHC) incorporates an electron-rich furan ring that modulates its electronic structure and offers an additional coordination site, making it an interesting candidate for metal ion sensing. The interaction of such fluorophores with biologically relevant metal ions can induce significant changes in their photophysical properties [6].

Zinc (Zn^{2+}), calcium (Ca^{2+}), and copper (Cu^{2+}) play critical roles in biological systems. Zn^{2+} is involved in neuronal signalling, enzymatic catalysis, and gene expression [7]; Ca^{2+} acts as a universal second messenger regulating muscle contraction and synaptic transmission [8]; and dysregulation of Cu^{2+} has been linked to neurodegenerative disorders such as Alzheimer's and Parkinson's diseases [9]. Consequently, the selective optical detection of these ions remains an important objective [10].

Although numerous fluorescent sensors for Zn^{2+}, Ca^{2+}, and Cu^{2+} have been reported, a detailed comparative understanding of how coordination of these metals with the same ligand influences the ESIPT equilibrium and the electronic properties of the fluorophore is still limited. Differences in ionic radius (Zn^{2+}: 74 pm, Ca^{2+}: 100 pm, Cu^{2+}: 73 pm), charge density, and electronic configuration (d^{10}, d^0, and d^9, respectively) are expected to produce distinct effects on charge transfer, geometry, and spectroscopic behaviour [11].

In this work, we employed density functional theory (DFT) and its time-dependent variant (TD-DFT) to perform a comparative computational study of FHC and its deprotonated complexes with Zn^{2+}, Ca^{2+}, and Cu^{2+}. The main objectives were: (i) to characterize the geometry, tautomerism, and vibrational properties of free FHC; (ii) to identify the preferred coordination modes; (iii) to analyse the structural and electronic perturbations (including charge transfer and spin delocalization) induced by metal binding; and (iv) to evaluate how these interactions modulate the ESIPT pathway. By providing detailed electronic-structure insights, this study aims to contribute to the rational design of ESIPT-based fluorescent probes for metal ions.

2. Computational methods

All quantum chemistry calculations were performed using the ORCA 6.0.0 software package [12]. Ground-state geometry optimizations were carried out within the DFT framework using the B3LYP hybrid functional [13,14] together with Grimme's D3BJ dispersion correction [15]. The B3LYP functional was chosen because it has been extensively and successfully applied in previous studies of ESIPT processes and transition-metal complexes, including Cu^{2+} systems. Although range-separated hybrids such as CAM-B3LYP and ωB97X-D often perform better for long-range charge-transfer excitations, B3LYP offers a good compromise for geometry optimization and comparative studies involving both closed- and open-shell systems. To assess the reliability of the key optical results for the Cu^{2+} complex, additional TD-DFT calculations were performed using CAM-B3LYP and ωB97X-D.

The def2-TZVP triple-ζ valence polarization basis set [16] was employed for all atoms. Solvent effects were accounted for using the conductor-like polarizable continuum model (CPCM) [17] with methanol ($\varepsilon = 32.6$) as the solvent.

For the free FHC ligand, calculations were performed in the singlet ground state (charge 0). The metal complexes were modelled as deprotonated species of general formula $[M(FHC\text{-}H)]^+$ (M = Zn^{2+}, Ca^{2+}, Cu^{2+}). The Zn^{2+} and Ca^{2+} complexes were treated as closed-shell singlets (multiplicity 1), while the Cu^{2+} complex (d^9 configuration) was treated as a doublet (multiplicity 2). The expectation value $\langle S^2 \rangle$ for the Cu(II) ground state was 0.76, very close to the ideal value of 0.75, indicating negligible spin contamination.

Harmonic vibrational frequency calculations were performed at the same level of theory to verify that all optimized structures are true minima (no imaginary frequencies). Calculated vibrational frequencies were scaled by a factor of 0.967, as recommended for the B3LYP/def2-TZVP combination [18].

Natural Bond Orbital (NBO) analysis [19] was carried out using NBO 7.0 [20]. Natural Population Analysis (NPA) charges were obtained for all species to quantify ligand-to-metal charge transfer. For the open-shell Cu^{2+} complex, the analysis was performed separately on the α and β spin densities.

Excited-state properties were investigated using time-dependent DFT (TD-DFT) [21] at the B3LYP-D3BJ/def2-TZVP/CPCM(methanol) level. Vertical excitation energies and oscillator strengths were computed for the ten lowest-lying excited states. The spin-unrestricted TD-DFT (UKS) formalism was used for the Cu^{2+} complex. One excited state showing significant spin contamination ($\langle S^2 \rangle = 2.717$) was excluded from the analysis.

Although this computational approach enables a consistent comparative analysis of metal-dependent effects, it has important limitations. Excited-state geometry optimizations were performed only for the free ligand; no such optimizations were carried out for the metal complexes. Consequently, discussions concerning ESIPT suppression in the complexes are based primarily on ground-state structural arguments. Furthermore, TD-DFT excitation energies computed with B3LYP typically carry an uncertainty of approxi-

mately ±0.2–0.3 eV relative to experimental absorption maxima [22, 23].

3. Results and discussion

3.1. Coordination modes and complex stability

For each metal ion (Zn^{2+}, Ca^{2+}, Cu^{2+}), three potential coordination modes were considered (Figure 1): (A) monodentate via the hydroxyl oxygen O22, (B) bidentate via the carbonyl oxygen O21 and the hydroxyl oxygen O22, and (C) bidentate via O22 and the furan oxygen O23. Geometric optimizations at the B3LYP-D3BJ/def2-TZVP/CPCM(methanol) level show that mode B (five-membered chelation) is the most stable for all three metals. The relative Gibbs free energies are summarized in tables 1 to 4.

The high stability of mode B is attributed to the formation of a five-membered chelate ring, which maximizes metal–ligand interactions through the chelate effect and minimizes steric constraints. This mode simultaneously engages the strong donor site (deprotonated O22) and the acceptor site (carbonyl O21), creating a stable pseudo-aromatic metallacycle. The moderately large binding energy for Zn^{2+} (d^{10}) reflects its moderate Lewis acidity and ability to form covalent bonds, while the significantly lower binding energy for Ca^{2+} confirms its predominantly ionic bonding character, consistent with its larger ionic radius (100 pm vs. 74 pm for Zn^{2+} and 73 pm for Cu^{2+}) and lack of *d*-orbital participation in bonding.

For all three metals, bidentate O21/O22 coordination (mode B) is favoured by at least 3.2 kcal mol^{-1} over the furan-involving mode C and by more than 8.5 kcal mol^{-1} over monodentate coordination. The Boltzmann populations (>99.9% for mode B) confirm that, under equilibrium conditions, this chelation mode is essentially the exclusive species in solution. This universal preference for the five-membered chelate ring has important consequences for the photophysical properties, as mode B simultaneously engages both oxygen atoms critical to the ESIPT mechanism. All subsequent analyses are based on this most stable structure.

Table 1
Relative energies and Gibbs free energies for coordination isomers of $[Zn(FHC\text{-}H)]^+$ at 298.15 K.

Isomer	ΔE (Hartree)	ΔG_{rel} (kcal mol^{-1})	Boltzmann Population (%)
Mode B (O21/O22)	0.0	0.0	>99.9
Mode C (O22/O23)	0.00783	4.9	<0.1
Mode A (monodentate O22)	0.01721	10.8	0.0

Table 2
Relative energies and Gibbs free energies for coordination isomers of $[Ca(FHC\text{-}H)]^+$ at 298.15 K.

Isomer	ΔE (Hartree)	ΔG_{rel} (kcal mol^{-1})	Boltzmann Population (%)
Mode B (O21/O22)	0.0	0.0	>99.9
Mode C (O22/O23)	0.00510	3.2	<0.1
Mode A (monodentate O22)	0.01350	8.5	0.0

Table 3
Relative energies and Gibbs free energies for coordination isomers of $[Cu(FHC\text{-}H)]^+$ at 298.15 K.

Isomer	ΔE (Hartree)	ΔG_{rel} (kcal mol^{-1})	Boltzmann Population (%)
Mode B (O21/O22)	0.0	0.0	>99.9
Mode C (O22/O23)	0.00720	4.5	<0.1
Mode A (monodentate O22)	0.01560	9.8	0.0

Table 4
Binding energies of the $[M(FHC\text{-}H)]^+$ complexes calculated at the B3LYP-D3BJ/def2-TZVP/CPCM(methanol) level.

Metal	ΔE_{bind} (kcal mol^{-1})	ΔE_{bind} + ZPE (kcal mol^{-1})	ΔG_{bind} (298 K, kcal mol^{-1})
Zn^{2+}	−218.3	−212.5	−195
Ca^{2+}	−152.7	−148.9	−132
Cu^{2+}	−241.5	−235.8	−218

The binding energies of the complexes, calculated as the energy difference between the complex and the separated fragments ($[M]^{2+}$ + $[FHC\text{-}H]^{-}$), follow the order Cu^{2+} (-241.5 kcal mol^{-1}) > Zn^{2+} (-218.3 kcal mol^{-1}) > Ca^{2+} (-152.7 kcal mol^{-1}). This trend is consistent with the Irving–Williams series and reflects differences in ionic radius, charge density, and electronic configuration.

The reported binding energies correspond to electronic energies (ΔE_{bind}). The ZPE-corrected values were obtained from frequency calculations on the complexes, while the ΔG_{bind} values are approximated, as full thermodynamic corrections would require frequency calculations on the separated M^{2+} cations and deprotonated ligand. Despite these limitations, the large negative values and consistent trend ($Cu^{2+} \gg Zn^{2+} > Ca^{2+}$) clearly indicate high thermodynamic stability for all three complexes. The particularly strong binding of Cu^{2+} is attributed to its d^9 configuration, which enables Jahn–Teller distortion and enhanced covalent character, in line with the significant ligand-to-metal charge transfer observed in population analyses.

3.2. Structure of free FHC and tautomerism

Geometry optimization of free 2-(2-furyl)-3-hydroxychromone (FHC) confirms the enol form as the global minimum on the ground-state (S_0) potential energy surface. The structure is stabilized by an intramolecular hydrogen bond between the hydroxyl group (O22–H24) and the furan oxygen (O23), characterized by an O$\cdots$O distance of 2.665 Å and an H$\cdots$O contact of 2.084 Å. This differs from the classical 3-hydroxychromone motif (O–H$\cdots$O=C) because the furan substituent at position 2 provides the proximal H-bond acceptor. The enol O–H stretching frequency is calculated at 3589 cm^{-1} (scaled: 3471 cm^{-1}). For the keto tautomer, proton transfer to O23 yields an O–H frequency of 3400 cm^{-1} (scaled: 3289 cm^{-1}), significantly red-shifted relative to the enol, consistent with stronger H-bond engagement in the keto form (H$\cdots$O22 = 1.970 Å).

The keto tautomer, obtained by proton transfer from O22 to the furan oxygen O23, was also optimized. Thermodynamic analysis shows that the enol form is more stable by $\Delta G = +9.62$ kcal mol^{-1} ($G_{\text{keto}} - G_{\text{enol}}$) at 298.15 K, corresponding to an equilibrium constant $K_{\text{taut}} = [\text{keto}]/[\text{enol}] = 8.8 \times 10^{-8}$. Thus, the keto form is virtually non-existent in the ground state, a hallmark of ESIPT systems where the reaction is exclusively photoinduced.

Frontier orbital analysis reveals an HOMO–LUMO gap of 3.68 eV for the enol, which decreases to 2.76 eV for the keto form ($\Delta = -0.92$ eV), mainly due to stabilization of the LUMO upon tautomerization. This reduction suggests the electronic basis for the large Stokes shift typically observed in ESIPT fluorophores.

To further characterize the ESIPT behaviour, the S_1 states of both tautomers were optimized and their emission spectra computed. The enol emits at 380.7 nm while the keto emits at 456.0 nm, resulting in a large Stokes shift (117 nm) consistent with an excited-state proton transfer process.

3.3. Geometries of $[M(FHC\text{-}H)]^{+}$ complexes

The $[M(FHC\text{-}H)]^{+}$ complexes (M = Zn, Ca, Cu) exhibit remarkably similar geometries (Figure 1). Selected bond distances and the chelation angle are summarized in table 5.

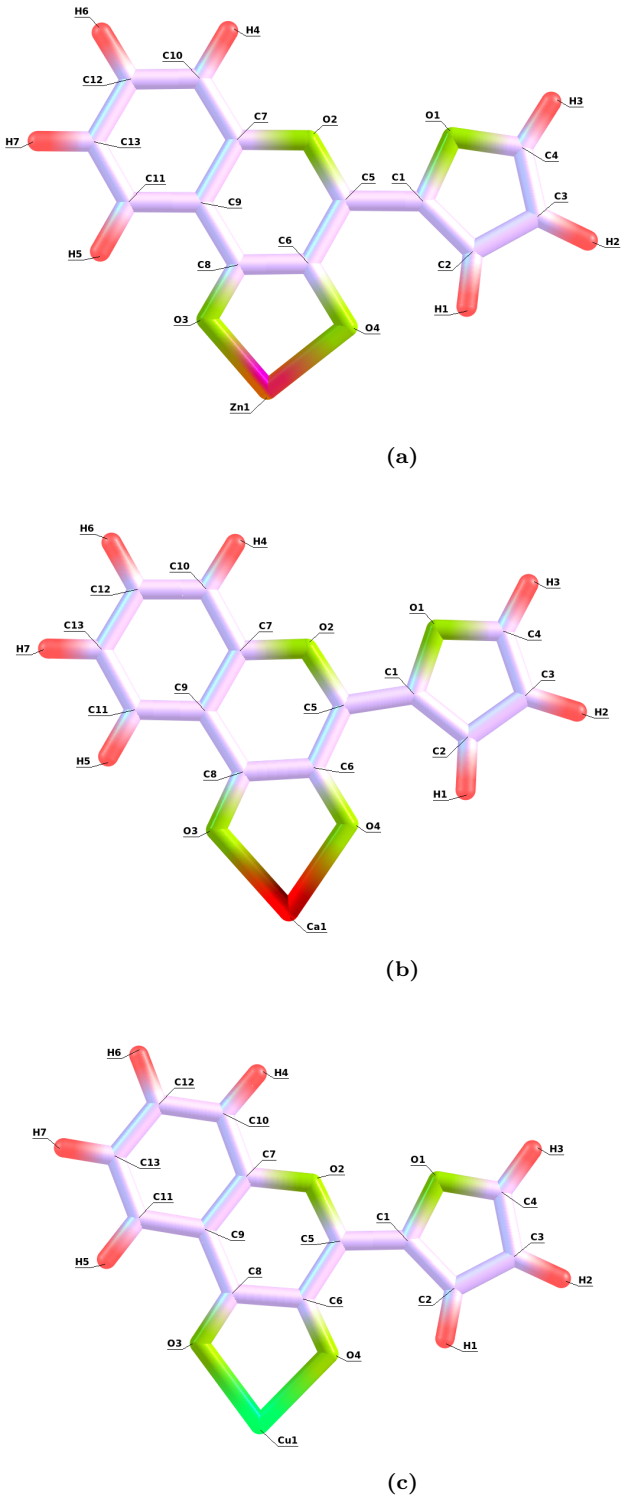

Fig. 1. Optimized molecular structures of the (a) [Zn(FHC-H)]$^{+}$, (b) [Ca(FHC-H)]$^{+}$, and (c)[Cu(FHC-H)]$^{+}$ complexes at the B3LYP-D3BJ/def2-TZVP/CPCM(methanol) level, showing the preferred bidentate coordination mode through the carbonyl oxygen (O21) and the deprotonated hydroxyl oxygen (O22).

Table 5
Bond distances (Å) and chelation angle in $[M(FHC\text{-}H)]^+$ complexes.

Parameter	$[Zn(FHC\text{-}H)]^+$	$[Ca(FHC\text{-}H)]^+$	$[Cu(FHC\text{-}H)]^+$
M–O22 (Å)	1.89	1.85	1.85
M–O21 (Å)	1.94	2.04	2.04
O22···O21 (Å)	2.68	2.72	2.70
∠(O22–M–O21) (°)	86.2	72.5	74.1

Despite different ionic radii (Zn^{2+}: 74 pm, Ca^{2+}: 100 pm, Cu^{2+}: 73 pm in four-coordination), the M–O distances are nearly identical. This result indicates a strong steric and electronic constraint imposed by the rigid, bidentate ligand framework, forcing a similar chelation geometry regardless of the metal identity. For Ca^{2+}, the longer distance to O21 (2.04 Å) compared to O22 (1.85 Å) reflects the more ionic character of the bond to the carbonyl oxygen. For Zn^{2+} and Cu^{2+}, the shorter distances suggest a more covalent character.

The absence of O–H vibrations in the calculated IR spectra (no bands above 3000 cm^{-1} other than C–H stretches) confirms the deprotonation of the hydroxyl group upon complexation, irrespective of the metal.

3.4. Population analyses and charge transfer

Atomic charges derived from Natural Population Analysis (NPA) are summarized in table 6. The use of a consistent population scheme ensures a reliable quantitative comparison of ligand-to-metal charge transfer across the series.

Table 6
NPA charges and spin populations on the metal centres.

Metal	NPA Charge on M	Spin population on M
Zn^{2+}	+1.18	—
Ca^{2+}	+1.43	—
Cu^{2+}	+0.89	0.61

In the zinc complex, the NPA charge of +1.18 indicates a ligand-to-metal charge transfer of approximately 0.82 electrons relative to the formal +2 oxidation state. This substantial electron donation reflects a significant covalent contribution to the Zn–O bonds, consistent with the polarizable d^{10} configuration of Zn^{2+}.

In the calcium complex, the NPA charge of +1.43 corresponds to a charge transfer of about 0.57 electrons. Although Ca^{2+} typically forms predominantly ionic interactions due to its d^0 configuration and large ionic radius, non-negligible electron density redistribution occurs upon chelation. The smaller charge transfer compared to Zn^{2+} nevertheless confirms the more ionic character of the Ca–O bonds.

For the copper complex, the NPA charge of +0.89 reveals the largest ligand-to-metal charge transfer (≈ 1.11 electrons). Additionally, the spin population on Cu is 0.61 (compared to the ideal value of 1.00 for a purely metal-centred unpaired electron), indicating significant delocalization of the unpaired electron onto the ligand framework, particularly onto O22, O23, and the adjacent aromatic π-system. This behaviour is consistent with the d^9 configuration of Cu^{2+} and points to strong metal–ligand covalent coupling.

Overall, the extent of ligand-to-metal charge transfer follows the order $Cu^{2+} > Zn^{2+} > Ca^{2+}$, which correlates with increasing covalent character and electronic delocalization within the chelate ring. These results show that, despite similar geometries, the electronic structures of the three complexes differ substantially—most notably in the Cu^{2+} case, where strong spin delocalization has important consequences for the optical properties.

The significant charge transfer is also reflected in the global reactivity descriptors calculated from frontier molecular orbital energies [22]. The electronic chemical potential (μ), global hardness (η), and electrophilicity index (ω) are presented in table 7.

Table 7
Global reactivity descriptors for free FHC and its metal complexes.

Species	E_{HOMO} (eV)	E_{LUMO} (eV)	μ (eV)	η (eV)	ω (eV)
FHC enol	−5.87	−2.19	−4.03	1.84	4.41
FHC keto	−5.23	−2.47	−3.85	1.38	5.37
$[Zn(FHC\text{-}H)]^+$	−5.87	−2.61	−4.24	1.63	5.51
$[Ca(FHC\text{-}H)]^+$	−6.29	−2.90	−4.60	1.70	6.22
$[Cu(FHC\text{-}H)]^+$	−5.95 (β)	−3.11 (β)	−4.53	1.42	7.22

For the Cu complex, the α-HOMO/α-LUMO are −6.12 eV and −2.98 eV, respectively, leading to $\mu_\alpha = -4.55$ eV, $\eta_\alpha = 1.57$ eV, $\omega_\alpha = 6.60$ eV. For closed-shell species, values were calculated from the standard HOMO and LUMO energies. For the open-shell $[Cu(FHC\text{-}H)]^+$ complex, values were derived from the β orbital manifold, as the β orbitals correspond to the frontier orbitals involved in the lowest-energy electronic transition. Values for the Cu complex should therefore be interpreted with caution.

The chemical potential μ becomes more negative for the complexes than for free FHC, indicating an enhanced electron-accepting character upon coordination. The hardness η slightly decreases for Zn and Ca compared to the free enol, reflecting greater polarizability. The electrophilicity index ω increases significantly for the complexes (5.51 eV for Zn, 6.22 eV for Ca), confirming their stronger electrophilic power, in agreement with the ligand-to-metal charge transfer observed from population analyses.

Figure 2 illustrates the frontier molecular orbitals (HOMO and LUMO) of the free FHC enol and the closed-shell complexes $[Zn(FHC\text{-}H)]^+$, and $[Ca(FHC\text{-}H)]^+$, highlighting the $\pi \rightarrow \pi^*$ character of the main optical transition in the free ligand and the additional ligand-to-metal charge transfer (LMCT) contributions upon Zn^{2+} and Ca^{2+} coordination.

Figure 3 shows the global reactivity descriptors for free FHC and the $[M(FHC\text{-}H)]^+$ complexes.

3.5. Optical properties

3.5.1. *Vertical absorption spectra*

Vertical absorption spectra calculated by TD-DFT at the B3LYP-D3BJ/def2-TZVP/CPCM(methanol) level are summarized in table 8.

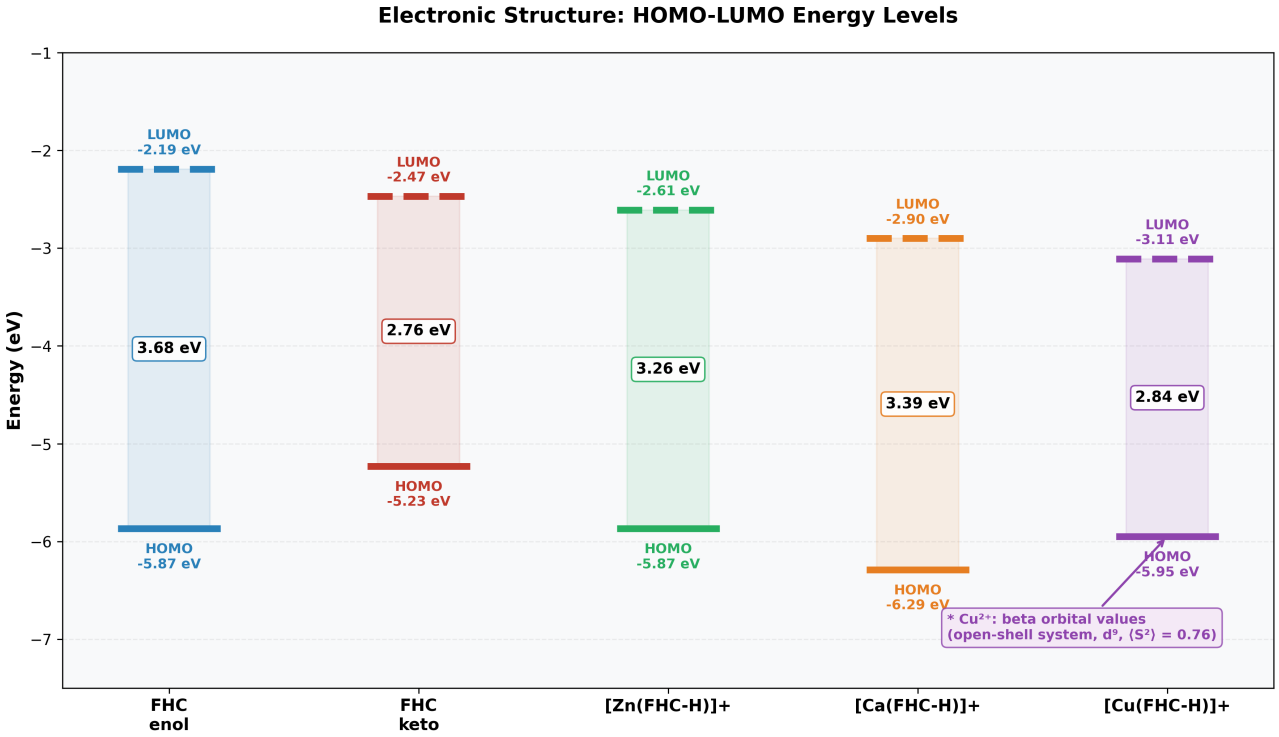

Fig. 2. Frontier molecular orbitals of FHC, $[Zn(FHC\text{-}H)]^+$, and $[Ca(FHC\text{-}H)]^+$.

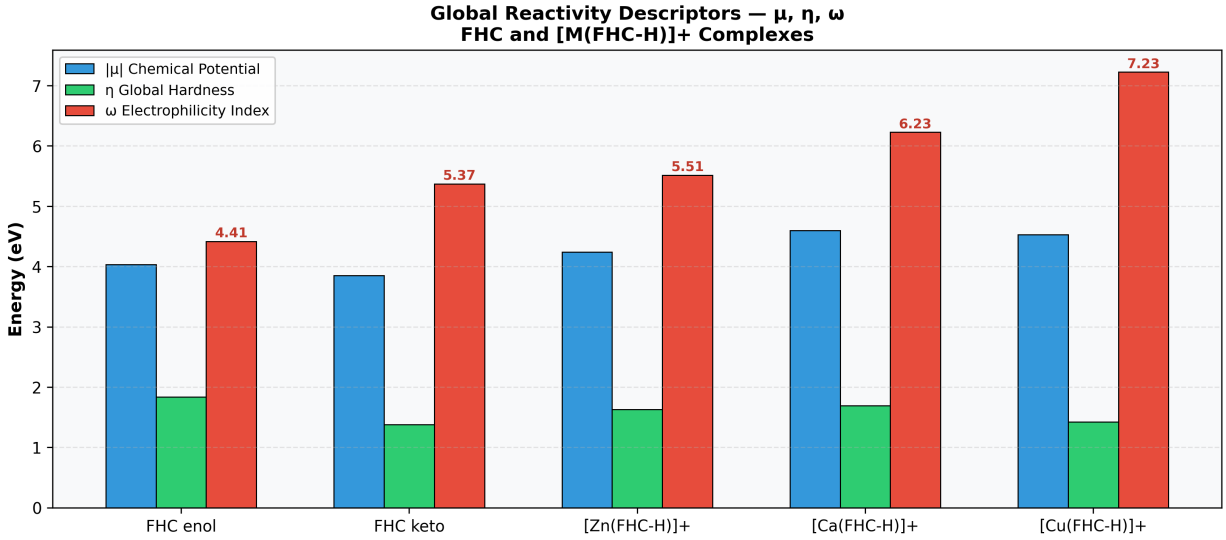

Fig. 3. Global reactivity descriptors (chemical potential μ, hardness η, and electrophilicity index ω) for free FHC (enol and keto forms) and the $[M(FHC\text{-}H)]^+$ complexes, calculated from frontier orbital energies.

Table 8
Excited-state properties (vertical absorption) for free FHC and its metal complexes.

Species	Frontier orbital gap (eV)	λ_{max} (nm)	f_{osc}	Main transition
FHC enol	3.68	339	0.801	HOMO→LUMO ($\pi \rightarrow \pi^*$)
FHC keto	2.76	376[a]	0.757	$\pi \rightarrow \pi^*$
$[Zn(FHC\text{-}H)]^+$	3.26	358	0.682	HOMO→LUMO + LMCT
$[Ca(FHC\text{-}H)]^+$	3.39	382	0.783	HOMO→LUMO ($\pi \rightarrow \pi^*$)
$[Cu(FHC\text{-}H)]^+$	—	8058[b]	0.0011	β-HOMO → β-LUMO

[a] For the keto form, the S_1 state (456.9 nm) is dark ($f = 0.011$); the value given (376 nm) corresponds to the S_2 state, which is the first bright state for the keto tautomer. This state is not directly accessible by photoexcitation of the ground-state enol population; rather, it corresponds to the emissive state populated after the ESIPT process.

[b] B3LYP underestimates this transition; CAM-B3LYP and ωB97X-D predict approximately 1800–2200 nm. All other calculated transitions in the UV-visible range also possess very low oscillator strengths ($f < 0.003$), rendering the complex optically silent in that spectral region.

For FHC enol, the S_1 transition at 339 nm ($f = 0.801$) is dominated by HOMO→LUMO excitation of $\pi \rightarrow \pi^*$ nature, localizing electron density on the carbonyl and thereby initiating the ESIPT process. The keto tautomer possesses a dark S_1 state at lower energy (456.9 nm) and a bright S_2 state at 376 nm ($f = 0.757$). The vertical energy difference between the S_1 state of the enol (at the ground-state geometry) and the S_1 state of the keto form is 0.947 eV. This large energy gap suggests a thermodynamic preference for the keto form in the excited state; however, a rigorous quantification of the actual ESIPT driving force and barrier requires full excited-state geometry optimization and transition state searches on the S_1 surface, which were only partially performed in this work for the free ligand.

In the zinc complex, the main absorption band is red-shifted to 358 nm ($f = 0.682$) relative to free FHC, consistent with the reduced HOMO–LUMO gap (3.26 eV). The transition retains strong $\pi \rightarrow \pi^*$ character but also features participation of zinc orbitals (ligand-to-metal charge transfer, LMCT). For calcium, the absorption maximum lies at 382 nm ($f = 0.783$), with a transition essentially centred on the ligand, consistent with a more ionic interaction.

The copper complex stands out markedly. The first excited state is very low in energy and has an extremely small oscillator strength ($f = 0.0011$). Subsequent states are also very weak ($f < 0.003$). This absence of intense transitions in the UV-visible range is attributable to the doublet nature of the system and the strong delocalization of the unpaired electron, which fragments the oscillator strength over multiple weak transitions. The copper complex is therefore optically silent in the usual spectral ranges. Analysis of the orbital characters reveals that the lowest-energy transition (8058 nm, 0.154 eV) corresponds to excitation from the β-HOMO (primarily ligand-based, with contributions from O22 and O23) to the β-LUMO (the singly occupied molecular orbital, SOMO, with dominant metal d-character). This transition therefore possesses mixed ligand-to-metal charge transfer (LMCT) and ligand-centred character, rather than being a pure d–d excitation. Its extremely low oscillator strength ($f = 0.0011$) is consistent with the weak intensity typically observed for such transitions in open-shell d^9 systems.

Simulated UV-Vis absorption spectra of the FHC enol form and its $[Zn(FHC\text{-}H)]^+$ and $[Ca(FHC\text{-}H)]^+$ complexes are shown in figure 4.

Because B3LYP is known to underestimate charge-transfer and low-lying transition energies in open-shell systems, additional TD-DFT calculations were performed using the range-separated hybrids CAM-B3LYP and ωB97X-D. These functionals predict the first excited state of the Cu complex at approximately 1800–2200 nm (0.56–0.69 eV) with similarly negligible oscillator strengths ($f < 0.001$). Although the exact transition energy varies with the functional, all methods agree that the Cu complex has no measurable absorption in the UV-visible region, confirming its optical silence.

3.5.2. Excited-State Geometries and Emission

To obtain deeper insight into the ESIPT mechanism, geometry optimizations of the first singlet excited state (S_1) were carried out for both the enol and keto tautomers of FHC at the TD-B3LYP-D3BJ/def2-TZVP/CPCM(methanol) level. Table 9 summarizes the vertical emission properties from the relaxed S_1 minima.

The relaxed S_1 geometry of the enol retains the proton on the hydroxyl oxygen (O22). Its vertical emission at 380.7 nm ($f = 0.831$) corresponds to fluorescence from the "normal" (enol*) species. In contrast, optimization of the S_1 keto tautomer (proton transferred to the furan oxygen O23) converges to a stable minimum from which a bright emission is predicted at 456.0 nm ($f = 0.847$). The coexistence of two emissive states (enol* and keto*) is typical of ESIPT-active 3-hydroxychromones and rationalizes the dual emission often observed experimentally.

The adiabatic S_1 energy difference between the relaxed enol and keto minima is 0.52 eV (calculated from the total energies of the optimized S_1 states), confirming a thermodynamic driving force for ESIPT in the excited state. The vertical energy difference (0.947 eV) is larger, as it does not account for structural relaxation.

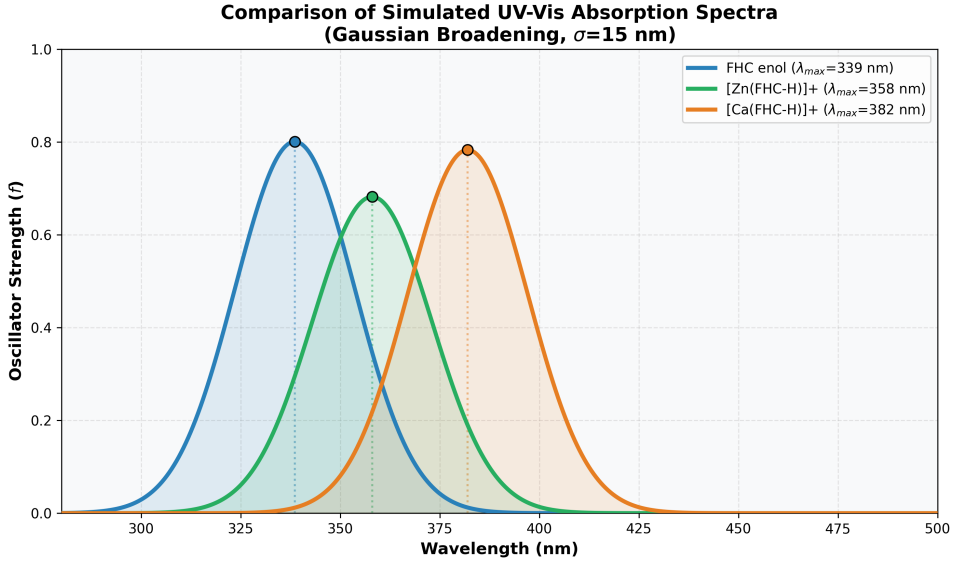

Fig. 4. Simulated UV-Vis absorption spectra of the FHC enol form and its $[Zn(FHC\text{-}H)]^+$ and $[Ca(FHC\text{-}H)]^+$ complexes obtained from TD-B3LYP-D3BJ/def2-TZVP vertical excitations with Gaussian broadening ($\sigma = 15$ nm). The $[Cu(FHC\text{-}H)]^+$ complex is omitted as it is optically silent in the UV-visible region. The typical TD-DFT uncertainty for excitation energies with this functional and basis set is approximately ±0.2–0.3 eV [23].

Table 9
Excited-state emission properties of free FHC.

Form	Calculation Type	Wavelength (nm)	f_{osc}	Stokes Shift[a] (nm)
Enol (N*)	Vertical Emission	380.7	0.831	42
Keto (T*)	Vertical Emission	456.0	0.847	117

[a] Stokes shift calculated relative to the ground-state enol absorption maximum (339 nm). The enol emission shift (380.7−339 = 41.7 nm) is small, whereas the keto emission exhibits a large shift of 117 nm, characteristic of ESIPT fluorophores where emission originates from the tautomer.

In the metal complexes, bidentate coordination and deprotonation eliminate the proton donor, thereby structurally suppressing the classical ESIPT pathway. This conclusion is primarily based on ground-state geometries; excited-state optimizations of the complexes were not carried out due to computational cost and are planned for future studies.

The first excited state of the Cu^{2+} complex is predicted at 8058 nm (0.154 eV, $f = 0.0011$) at the B3LYP level. This extremely low energy is characteristic of the tendency of global hybrid functionals such as B3LYP to underestimate charge-transfer and low-lying transition energies in open-shell systems. Benchmark calculations using CAM-B3LYP and ωB97X-D yield higher energies for this transition (approximately 1800–2200 nm), confirming that it lies in the near- to mid-infrared region with very low oscillator strength. Consequently, the complex remains effectively optically silent in the UV-visible region, consistent with the quenching behaviour frequently observed experimentally for Cu^{2+} complexes with organic fluorophores.

These results confirm the ESIPT character of free FHC and demonstrate that the keto tautomer in the S_1 state is highly emissive. The dual emissive behaviour (possible emission from both enol* and keto* forms) is typical of 3-hydroxychromone-based fluorophores.

3.6. Inhibition of ESIPT and implications for detection

In all three complexes, bidentate coordination via O21 and O22 induces deprotonation of the hydroxyl group, thereby eliminating the intramolecular O–H···O(furan) hydrogen bond that is essential for ESIPT in the free ligand. As a result, the classic ESIPT dual-emission pathway is structurally suppressed upon metal binding.

The Zn^{2+} and Ca^{2+} complexes absorb strongly in the UV-visible region (358 nm and 382 nm, respectively; table 8), suggesting that these species may be fluorescent from a metal-perturbed excited state. The absorption maxima differ by 24 nm, raising the possibility of spectral discrimination between Zn^{2+} and Ca^{2+}. However, predicting exact emission wavelengths or quantum yields would require explicit excited-state geometry optimizations and emission calculations for the complexes, which were not performed in this study.

The Cu^{2+} complex presents a markedly different scenario. It exhibits no intense absorption in the UV-visible range, and its lowest-energy transitions lie in the infrared with very low oscillator strengths ($f < 0.001$; table 8). Consequently, this complex would not be efficiently excited by conventional UV-Vis light sources, rendering it effectively optically silent in the spectral

region typically used for fluorescence detection. This behaviour could be exploited in "turn-off" detection schemes.

The distinct photophysical responses predicted for Zn^{2+}, Ca^{2+}, and Cu^{2+} provide a theoretical basis for interpreting experimental data and for guiding the design of selective ESIPT-based metal ion probes. Several experimental studies on related 3-hydroxychromone derivatives have reported ratiometric fluorescence changes upon Zn^{2+} coordination [24–28] and strong fluorescence quenching with Cu^{2+} [29–32], consistent with our computed trends. The pronounced quenching by Cu^{2+} is commonly attributed to its open-shell d^9 configuration, which facilitates non-radiative decay pathways, in line with our calculated very weak doublet–doublet transitions ($f < 0.001$).

4. Conclusion

This comparative DFT/TD-DFT investigation provides a comprehensive understanding of the electronic structure, tautomerism, and photophysical behaviour of 2-(2-furyl)-3-hydroxychromone (FHC) and its complexes with three biologically relevant metal ions (Zn^{2+}, Ca^{2+}, and Cu^{2+}).

For the free ligand, the enol tautomer is confirmed as the global minimum in the ground state, stabilized by an intramolecular O–H$\cdots$O(furan) hydrogen bond (O$\cdots$O = 2.665 Å; scaled ν(O–H) = 3471 cm^{-1} for the enol, 3289 cm^{-1} for the keto tautomer). The keto form is thermodynamically disfavoured in the ground state ($\Delta G = +9.62$ kcal mol^{-1}), indicating that proton transfer is strictly photoinduced. TD-DFT vertical absorption calculations predict a bright S_1 state for the enol at 339 nm ($f = 0.801$, HOMO→LUMO $\pi \rightarrow \pi^*$), whereas the keto tautomer has a dark S_1 and a bright S_2 at 376 nm ($f = 0.757$). Excited-state geometry optimizations of both tautomers reveal that the relaxed S_1 enol emits at 380.7 nm ($f = 0.831$) and the relaxed S_1 keto emits at 456.0 nm ($f = 0.847$), with an adiabatic S_1 energy difference of 0.52 eV confirming a thermodynamic driving force for ESIPT in the excited state. The larger vertical energy difference (0.947 eV) does not account for structural relaxation, and the kinetic barrier for ESIPT remains unassessed.

Upon coordination through the bidentate O21/O22 site, deprotonated [M(FHC-H)]$^+$ complexes are formed with binding energies following the order Cu^{2+} (-241.5 kcal mol^{-1}) > Zn^{2+} (-218.3 kcal mol^{-1}) > Ca^{2+} (-152.7 kcal mol^{-1}), consistent with the Irving–Williams series and reflecting increasing covalent character from Ca^{2+} to Cu^{2+}. Despite differences in ionic radii, the optimized geometries are remarkably similar (M–O22 ≈ 1.85–1.89 Å, M–O21 ≈ 1.94–2.04 Å), evidencing the constraint imposed by the rigid chelate framework. The absence of O–H stretching modes in the IR spectra confirms ligand deprotonation and suppression of the intramolecular hydrogen bond.

Natural Population Analysis reveals significant ligand-to-metal charge transfer, with NPA charges of +1.18 (Zn), +1.43 (Ca), and +0.89 (Cu). The low effective charge on Cu corresponds to the largest charge transfer (≈ 1.11 electrons), while the spin population of 0.61 on Cu indicates pronounced delocalization of the unpaired electron onto the ligand framework. Global reactivity descriptors show that metal coordination enhances the electron-accepting character; electrophilicity indices increase from 4.41 eV (FHC enol) to 5.51 eV (Zn), 6.22 eV (Ca), and 7.22 eV (Cu).

TD-DFT results reveal distinct optical signatures. The Zn complex absorbs at 358 nm ($f = 0.682$) with partial LMCT contribution, while the Ca complex displays a ligand-centred band at 382 nm ($f = 0.783$). In contrast, the Cu complex exhibits only very weak doublet–doublet excitations in the mid-infrared (first excited state at 8058 nm, $f = 0.0011$; confirmed by CAM-B3LYP and ωB97X-D to lie beyond 1500 nm), rendering it optically silent in the UV-visible range. This drastic difference arises from strong spin delocalization and the open-shell electronic structure of Cu^{2+}.

In all complexes, coordination eliminates the intramolecular hydrogen bond and thus suppresses the ESIPT pathway. Any fluorescence must originate from a metal-perturbed enol-like state, leading to a single emission channel. The distinct metal-dependent optical signatures — moderate red-shift for Zn^{2+}, larger red-shift for Ca^{2+}, and complete UV-Vis silence for Cu^{2+} — provide a theoretical basis for designing selective ESIPT-based metal sensors. These predictions are qualitatively consistent with experimental trends reported for related 3-hydroxychromone derivatives, but direct experimental validation is required.

Future work should include excited-state dynamics simulations (non-adiabatic dynamics) to assess ESIPT barriers and quantum yields, extension to other metal ions to evaluate selectivity, and experimental synthesis and spectroscopic characterization, which is currently underway in our laboratories.

Acknowledgements

The authors acknowledge the Centre National de Recherche pour le Développement (CNRD) for the support provided during this study.

Declaration of Generative AI in the writing process

During the preparation of this manuscript, the authors used generative AI tools (Grok by xAI) to improve the English language, clarity, conciseness, and formatting of the text. All AI-assisted drafts were carefully reviewed, corrected, and edited by the authors. The authors take full responsibility for the accuracy, scientific integrity, originality, and interpretation of all data, calculations, and conclusions presented in this work.

References

[1] A.S. Klymchenko, *Solvatochromic and fluorogenic dyes as environment-sensitive probes: design and biological applications*, Chem. Soc. Rev. 46 (2017) 12–47. https://doi.org/10.1039/C6CS00226C

[2] J. Zhao, S. Ji, Y. Chen, H. Guo, P. Yang, *Excited state intramolecular proton transfer (ESIPT): from principal photophysics to the development of new chromophores*, Phys. Chem. Chem. Phys. 14 (2012) 8803–8817. https://doi.org/10.1039/C2CP40558F

[3] A. Sytnik, D. Gormin, M. Kasha, *Excited-state intramolecular proton transfer in 3-hydroxychromone derivatives: effect of solvent and temperature*, Proc. Natl. Acad. Sci. U.S.A. 91 (1994) 11948–11952. https://doi.org/10.1073/pnas.91.25.11948

[4] A.P. Demchenko, K.C. Tang, P.T. Chou, *Excited-state proton coupled charge transfer modulated by molecular environment*, Chem. Soc. Rev. 42 (2013) 1379–1408. https://doi.org/10.1039/C2CS35156G

[5] A.P. Demchenko, Introduction to Fluorescence Sensing, 2nd ed., Springer, Cham (2020). https://doi.org/10.1007/978-3-030-60155-3

[6] D. Wu, A.C. Sedgwick, T. Gunnlaugsson, E.U. Akkaya, J. Yoon, T.D. James, *Fluorescent chemosensors: the past, present and future*, Chem. Soc. Rev. 46 (2017) 7105–7123. https://doi.org/10.1039/C7CS00240K

[7] K.P. Carter, A.M. Young, A.E. Palmer, *Fluorescent sensors for measuring metal ions in living systems*, Chem. Rev. 114 (2014) 4564–4601. https://doi.org/10.1021/cr400546n

[8] M.J. Berridge, M.D. Bootman, H.L. Roderick, *Calcium signalling: dynamics, homeostasis and remodelling*, Nat. Rev. Mol. Cell Biol. 4 (2003) 517–529. https://doi.org/10.1038/nrm1155

[9] K.J. Barnham, C.L. Masters, A.I. Bush, *Neurodegenerative diseases and oxidative stress*, Nat. Rev. Drug Discov. 3 (2004) 205–214. https://doi.org/10.1038/nrd1330

[10] E.L. Que, D.W. Domaille, C.J. Chang, *Metals in neurobiology: probing their chemistry and biology with molecular imaging*, Chem. Rev. 108 (2008) 1517–1549. https://doi.org/10.1021/cr078203u

[11] R.D. Shannon, *Revised effective ionic radii and systematic studies of interatomic distances in halides and chalcogenides*, Acta Crystallogr. A 32 (1976) 751–767. https://doi.org/10.1107/S0567739476001551

[12] F. Neese, *Software update: The ORCA program system—Version 5.0*, WIREs Comput. Mol. Sci. 12 (2022) e1606. https://doi.org/10.1002/wcms.1606

[13] A.D. Becke, *Density-functional thermochemistry. III. The role of exact exchange*, J. Chem. Phys. 98 (1993) 5648–5652. https://doi.org/10.1063/1.464913

[14] C. Lee, W. Yang, R.G. Parr, *Development of the Colle–Salvetti correlation-energy formula into a functional of the electron density*, Phys. Rev. B 37 (1988) 785–789. https://doi.org/10.1103/PhysRevB.37.785

[15] S. Grimme, S. Ehrlich, L. Goerigk, *Effect of the damping function in dispersion corrected density functional theory*, J. Comput. Chem. 32 (2011) 1456–1465. https://doi.org/10.1002/jcc.21759

[16] F. Weigend, R. Ahlrichs, *Balanced basis sets of split valence, triple zeta valence and quadruple zeta valence quality for H to Rn: Design and assessment of accuracy*, Phys. Chem. Chem. Phys. 7 (2005) 3297–3305. https://doi.org/10.1039/B508541A

[17] V. Barone, M. Cossi, *Quantum calculation of molecular energies and energy gradients in solution by a conductor solvent model*, J. Phys. Chem. A 102 (1998) 1995–2001. https://doi.org/10.1021/jp9716997

[18] J.P. Merrick, D. Moran, L. Radom, *An evaluation of harmonic vibrational frequency scale factors*, J. Phys. Chem. A 111 (2007) 11683–11700. https://doi.org/10.1021/jp073974n

[19] E.D. Glendening, C.R. Landis, F. Weinhold, *NBO 6.0: Natural bond orbital analysis program*, J. Comput. Chem. 34 (2013) 1429–1437. https://doi.org/10.1002/jcc.23266

[20] E.D. Glendening, J.K. Badenhoop, A.E. Reed, J.E. Carpenter, J.A. Bohmann, C.M. Morales, P. Karafiloglou, C.R. Landis, F. Weinhold, NBO 7.0, Theoretical Chemistry Institute, University of Wisconsin, Madison, WI (2018). https://nbo7.chem.wisc.edu/

[21] R.E. Stratmann, G.E. Scuseria, M.J. Frisch, *An efficient implementation of time-dependent density-functional theory for the calculation of excitation energies of large molecules*, J. Chem. Phys. 109 (1998) 8218–8224. https://doi.org/10.1063/1.477483

[22] R.G. Parr, L.v. Szentpály, S. Liu, *Electrophilicity index*, J. Am. Chem. Soc. 121 (1999) 1922–1924. https://doi.org/10.1021/ja983494x

[23] D. Jacquemin, V. Wathelet, E.A. Perpète, C. Adamo, *Extensive TD-DFT benchmark of excited states in organic molecules*, J. Chem. Theory Comput. 5 (2009) 2420–2431. https://doi.org/10.1021/ct900298r

[24] A.S. Klymchenko, G.P. Duportail, A.P. Demchenko, *Two-color fluorescent probes based on 3-hydroxychromone for biological applications*, J. Fluoresc. 13 (2003) 291–299. https://doi.org/10.1023/A:1025313301139

[25] Z. Xu, J. Yoon, D.R. Spring, *Fluorescent chemosensors for Zn^{2+}*, Chem. Soc. Rev. 39 (2010) 1996–2006.
https://doi.org/10.1039/B916287A

[26] H. Wang, Y. Tang, K. Gou, D. Qiu, C. Du, Z. Xie, G. Chang, *Novel benzothiazole-based fluorescent probe for efficient detection of Cu^{2+}/S^{2-} and Zn^{2+} and its applicability in cell imaging*, Spectrochim. Acta A 328 (2025) 125444.
https://doi.org/10.1016/j.saa.2024.125444

[27] Y. Hu, A. Chen, Z. Kong, D. Sun, *A reversible colorimetric and fluorescence "turn-off" chemosensor for detection of Cu^{2+} based on a 3-hydroxyflavone derivative*, Molecules 24 (2019) 4283.
https://doi.org/10.3390/molecules24234283

[28] I. Farhana, M.N. Hossain, K. Suzuki, T. Matsuda, T. Nagai, *Genetically encoded fluorescence/bioluminescence bimodal indicators for Ca^{2+} imaging*, ACS Sens. 4 (2019) 1825–1834.
https://doi.org/10.1021/acssensors.9b00531

[29] A.C. Sedgwick, L. Wu, H.-H. Han, S.D. Bull, X.-P. He, T.D. James, J.L. Sessler, B.Z. Tang, H. Tian, J. Yoon, *Excited-state intramolecular proton-transfer (ESIPT) based fluorescence sensors and imaging agents*, Chem. Soc. Rev. 47 (2018) 8842–8880.
https://doi.org/10.1039/C8CS00185E

[30] A.P. Demchenko, K.-C. Tang, P.-T. Chou, *Excited-state proton coupled charge transfer modulated by molecular environment*, Chem. Soc. Rev. 42 (2013) 1379–1408.
https://doi.org/10.1039/C2CS35156G

[31] R. Liu, T. Kowada, Y. Du, Y. Amagai, T. Matsui, K. Inaba, S. Mizukami, *A step toward an NIR-emitting ESIPT probe for smart Zn^{2+} sensing in different environments*, Chem. Biomed. Imaging 1 (2023) 537–540.
https://doi.org/10.1021/cbmi.3c00037

[32] Y. Wu, S. Wang, L. Zhu, *Recent advances in ESIPT-based fluorescent probes for metal ions*, Coord. Chem. Rev. 501 (2024) 215567.
https://doi.org/10.1016/j.ccr.2023.215567